Noname manuscript No.
(will be inserted by the editor)

Surface Thermal Heterogeneities and the Atmospheric Boundary Layer: the Relevance of Dispersive Fluxes

Fabien Margairaz* · Eric R. Pardyjak · Marc Calaf

Received: DD Month YEAR / Accepted: DD Month YEAR

Abstract While the increasing availability of computational power is enabling finer grid resolutions in numerical-weather-prediction models, representing land–atmosphere exchange processes remains challenging. This partially results from the fact that land-surface heterogeneity exists at all spatial scales, and its variability does not necessarily 'average' out with decreasing size. The work presented here uses large-eddy simulations and the concept of dispersive fluxes to quantify the effects of a surface that is thermally inhomogeneous (with scales that are approximately 10% of the height of the atmospheric boundary layer), but for uniformly rough. These near-canonical cases describe inhomogeneous scalar transport over a broad range of unstable atmospheric flows. Results illustrate the existence of a regime where the mean flow is mostly driven by the surface thermal heterogeneities. In this regime, the contribution of the dispersive fluxes can account for more than 40% of the total sensible heat flux at 100 m above the ground and about 5–10% near the surface. This result is independent of the spatial distribution of the thermal heterogeneities and weakly dependent on the averaging time used to define the dispersive fluxes. Additionally, an alternative regime exists where the effects of the surface thermal heterogeneities are quickly blended and the dispersive fluxes match those obtained over an equivalent homogeneous surface. Results further illustrate the existence of a new cospectral scaling for the dispersive sensible heat fluxes that differs from the traditional turbulence cospectral scal-

Fabien Margairaz
Department of Mechanical Engineering, University of Utah, Salt Lake City, Utah, USA
E-mail: fabien.margairaz@utah.edu

Eric R. Pardyjak
Department of Mechanical Engineering, University of Utah, Salt Lake City, Utah, USA

Marc Calaf
Department of Mechanical Engineering, University of Utah, Salt Lake City, Utah, USA
E-mail: marc.calaf@utah.edu

ing. We believe that these results might elucidate pathways for developing new parametrizations for the non-canonical atmospheric surface layer.

Keywords Large-eddy simulation, Scalar transport, Sensible heat flux, Surface temperature

1 Introduction

While advances in computation (and computing) are enabling finer grid resolutions in numerical-weather-prediction (NWP) models, representing land–atmosphere exchange processes as a lower boundary condition remains a challenge (regardless of the numerical resolution but not independent from it). Because land-surface heterogeneity exists at all spatial scales and does not necessarily 'average out' with decreasing size, its variability is not rapidly blended away from the boundary. Thus, it greatly affects the atmospheric surface layer (ASL). The induced mixing and forcing processes are characterized by short time scales ($\mathcal{O}(1$ h$)$) and limited spatial extent ($\mathcal{O}(100$ m$)$) that fall within the 'terra-incognita' range (Wyngaard 2004; Beare 2014), making it difficult for traditional NWP models to capture them.

Figure 1 presents a conceptual schematic that illustrates the relationship between the different atmospheric flow scales, the land-surface heterogeneity scales, and the available numerical resolution, which has been used to guide the development of the present study. In Fig. 1, the abscissa represents the length scale of the surface thermal heterogeneities (l_h) and the ordinate the length scale of the flow dynamics (l_d). Four relevant length scales are represented on both coordinate axis, $\mathcal{O}(100$ m$)$ represents the smallest flow scales resolved in near-future high-resolution mesoscale models ($\Delta_{meso}^{H.resol}$), and $\mathcal{O}(100$ km$)$ the horizontal domain size (L_{meso}). Additionally, $\mathcal{O}(10$ m$)$ and $\mathcal{O}(1$ km$)$, represent the same corresponding length scales for high-resolution large-eddy simulations (LES) ($\Delta_{LES}^{H.resol}$ and L_{LES}). Moreover, the flow scales are identified as either numerically resolved (region shaded in blue) or parametrized for high-resolution mesoscale models (region shaded in yellow). An arc is placed at scales $\mathcal{O}(100$ m$)$. Within this arc and above the diagonal are regions where unresolved (in mesoscale models) fluid motions are much larger than the scales of heterogeneity ($l_d/l_h >> 1$). Here, the fluid flow senses the surface as homogeneous and traditional ASL formulations should be valid. Within the arc and below the diagonal, unresolved fluid motions are much smaller than the scales of heterogeneity ($l_d/l_h << 1$) and again the turbulence feels the surface as homogeneous and traditional ASL formulations should be valid. Within an uncertain zone along the diagonal, represented between the grey lines, the fluid motion scales are of the same order as the scales of heterogeneity (i.e., $l_d \sim l_h$). It is precisely this heterogeneous numerically unresolved zone that frames the scope of this work (region shaded in red). Much of this zone overlaps with anticipated increases in NWP resolution as well as the 'terra-incognita' (Wyngaard 2004; Beare 2014). It is also the zone that is most problematic for ASL similarity relations (Patton et al. 2005; Li and Bou-Zeid 2013) and has been

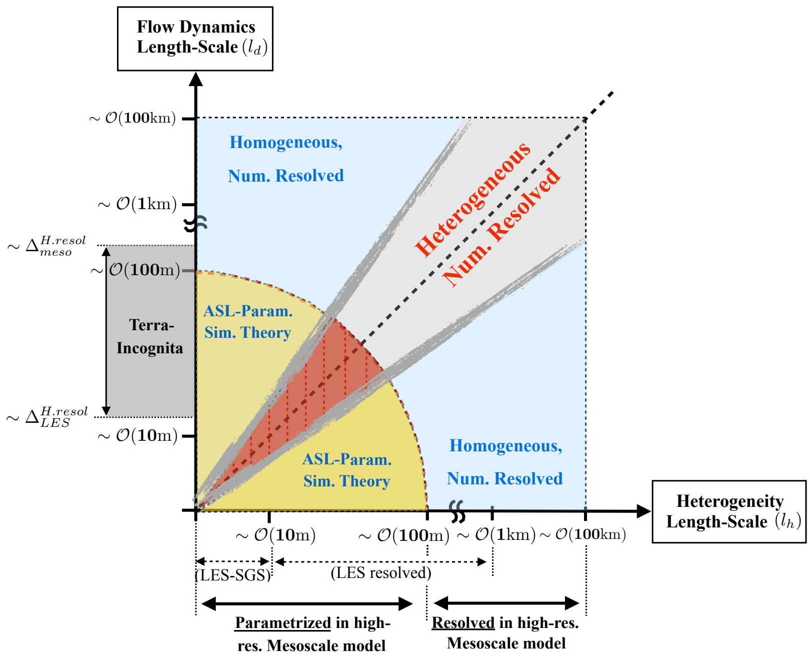

Fig. 1 Schematic of the interaction between turbulent eddies and heterogeneous surface patches of different scales illustrating the need for new ASL parametrizations in mesoscale modelling. The shaded regions represent different categories of turbulent scales: in blue, the scales are numerically resolved, and in yellow, the scales are parametrized for high-resolution mesoscale models. Between the grey lines is a region where eddy scales are of the same order as scales of heterogeneity (i.e., $l_e \sim l_h$). The region shaded in red represents the scope of this work

known as a source of error that is introduced by the indirect homogenization of surface spatial heterogeneities. This error depends on the numerical-model resolution, the characteristic length scale of the surface heterogeneities, and the parametrization used for the near-surface conditions (Patton et al. 2005; Li and Bou-Zeid 2013).

Because the flux–gradient similarity relationships were developed under the assumption of spatial homogeneity and statistical stationarity (Monin and Obukhov 1954; Stull 1988), prior efforts have attempted to overcome this inherent limitation using more or less sophisticated approaches to provide adjustments to the parametrization of the Reynolds-flux component of the sensible heat flux. Some examples of these strategies include the effective surface parameter approach (Wieringa 1986; Taylor 1987; Mason 1988; Claussen 1990; Wood and Mason 1991; Beljaars and Holtslag 1991; Bou-Zeid et al. 2004), the statistical-dynamical approach (Avissar 1991, 1992), and the mosaic and tile approaches (Avissar and Pielke 1989; Claussen 1991; Ament and Simmer 2006) or any modification of the ones above such as the extended tile (Blyth et al. 1993; Blyth 1995; Arola 1999). These methods are currently used in most NWP and climate models to parametrize surface energy fluxes over heterogeneous terrain because they are easy to implement and use, and due to the current lack of better alternatives. Further, the framework under which the tile and mosaic approaches should be used will become more severely challenged as numerical resolution increases because these methods were developed to be applied above the blending height. As additional compelling evidence of the limitations of these approaches in most heterogeneous cases, both methods lead to consistent overestimation of fluxes when used together with the flux–profile method (Stoll and Porté-Agel 2009).

As a first step towards developing new ASL parametrizations for high-resolution NWP models that overcome the problems presented above, the contribution of the dispersive fluxes is evaluated on flows over idealized thermally-heterogeneous surfaces with uniform roughness across a wide range of unstable stratification. The dispersive fluxes are representative of the spatial-averaging operation that explicitly represents the critical processes dependent on heterogeneity (Wilson and Shaw 1977; Raupach and Shaw 1982; Finnigan 1985; Raupach et al. 1986). They arise from the spatial averaging operator applied over a multiply-connected domain across solid–fluid interfaces (e.g. canopies) or they can be associated with the spatial variability of time-averaged quantities. The latter case is explored herein, where it is hypothesized that the thermal spatial heterogeneity of the land surface is generating important dispersive fluxes. A similar approach to the contribution of the time- and space-averaged fluxes was used in Kanda et al. (2004), Patton et al. (2005), Inagaki et al. (2006), Mauder et al. (2008), and Zhou et al. (2018) to analyze the closure problem of the energy balance, where it was found that part of the imbalance was due to the transport of heat by the mean vertical motion.

In Sect. 2, the derivation and theory related to the dispersive fluxes is reviewed; in Sect. 3, the numerical platform used and study cases are presented; Sect. 4 identifies the contribution of the dispersive fluxes and evaluates the work hypothesis indicated above; and Sect. 5 presents a spectral analysis of the fluxes. Finally, an extended discussion of the results, implications, and limitations of this work is provided in Sect. 6, with conclusions in Sect. 7.

2 Dispersive Fluxes

When the temporally-averaged equations of motion are spatially averaged, dispersive fluxes appear as an additional term that accounts for the effect of the spatial fluctuations of the time-averaged variables. As a result, dispersive fluxes quantify the spatial correlations of temporally-averaged quantities. Initially introduced by Wilson and Shaw (1977) and Raupach and Shaw (1982), dispersive fluxes can arise when a time-averaged variable ($\overline{u}_i$, with the overline representing time averaging) is represented as the sum of a time- and spatially-averaged variable ($\langle\overline{u}_i\rangle$, with the $\langle\cdot\rangle$ representing horizontal spatial averaging) with a time-averaged spatial deviation ($\overline{u}_i''$), for example,

$$\overline{u}_i = \langle\overline{u}_i\rangle + \overline{u}_i''. \tag{1}$$

Hence, by using this decomposition, which is the result of the spatial averaging of time-averaged variables, new covariances arise. These are the result of the spatial correlation of quantities averaged in time but varying with position. For example, the case for the heat fluxes may be written as

$$\langle \overline{w}''\overline{\theta}'' \rangle = \langle \overline{w}\,\overline{\theta} \rangle - \langle \overline{w} \rangle \langle \overline{\theta} \rangle. \tag{2}$$

Initially applied in atmospheric flows for the study of vegetated canopies (Wilson and Shaw 1977; Raupach and Thom 1981; Raupach and Shaw 1982; Raupach 1994; Finnigan 2000), dispersive fluxes have been shown to potentially play an important role in the description of spatially-averaged flow statistics (Poggi et al. 2004; Poggi and Katul 2008). Early work in this area indicated that dispersive fluxes are negligible in the mean flow outside canopies (Raupach et al. 1986; Cheng and Castro 2002). In contrast, Poggi et al. (2004) showed, using a flume study, that the contribution of the dispersive flux to the momentum fluxes could be larger than 10% in sparse canopies. Smaller dispersive fluxes of about 6% were also measured by Mignot et al. (2009) in flow over a gravel bed. However, Bailey and Stoll (2013) showed that, in sparse, row-oriented canopies, the dispersive flux was more than 20% of the magnitude of the turbulent flux. Similarly, a recent study demonstrated that dispersive fluxes are generated around canopy edges and that they can be large in the entry region of the canopy (Moltchanov et al. 2015). In addition, in urban-canopy studies, the contribution of dispersive fluxes has also been shown to be non-negligible (Martilli and Santiago 2007). For example, in LES studies of flow over random urban-like obstacles, the magnitude of the dispersive flux represents 15% of the magnitude of the turbulent flux, and the peak of the dispersive flux is located at the top of the canopy (Xie et al. 2008). These results have been confirmed in flow over realistic urban surfaces by Giometto et al. (2016). Similarly, studies of flow inside wind farms have shown that dispersive fluxes constitute a non-negligible fraction of the total vertical momentum flux (Calaf et al. 2010).

In the present study, the concept of dispersive fluxes is extended and applied to the sensible heat flux with two objectives in mind. First, as a means of accounting for the missing contribution to the surface energy budget resulting from persistent spatial thermal heterogeneities present in the time-averaged velocity and temperature fields. This is similar to the approach used by Kanda et al. (2004), Patton et al. (2005), Inagaki et al. (2006), Mauder et al. (2008), Zhou et al. (2018), and De Roo and Mauder (2018) to analyze the closure of the surface energy balance, where it was found that part of the energy imbalance was due to heat transport by the mean vertical motion. Second, as a potential means of developing new parametrizations for NWP models that inherently account for the effects of the unresolved thermal heterogeneities.

3 Numerical Simulations and Study Cases

The LES approach and details of the different study cases are briefly presented. A more detailed overview of the LES method can be found in Moeng and Sullivan (2015), and more details on the procedure used here can also be found in Bou-Zeid et al. (2004, 2005), Calaf et al. (2011), and Margairaz et al. (2018).

3.1 Large-Eddy Simulations Framework

In the LES method, the turbulent flow is separated into resolved and modelled scales. The resolved flow is obtained by numerically integrating the filtered incompressible Navier–Stokes equations. In the LES implementation used here, these equations are written in rotational form to ensure adequate conservation of energy by the inertial terms (Kravchenko and Moin 1997). Additionally, the momentum is coupled to the advection–diffusion equation of heat using the Boussinesq approximation. The dimensional form of the governing equations is therefore

$$\partial_i \tilde{u}_i = 0, \tag{3}$$

$$\partial_t \tilde{u}_i + \tilde{u}_j \left(\partial_j \tilde{u}_i - \partial_i \tilde{u}_j\right) = -\partial_i \tilde{p}^* - \partial_j \tau_{ij}^{\Delta,d} + g\left(\frac{\tilde{\theta} - \langle\tilde{\theta}\rangle_{xy}}{\langle\tilde{\theta}\rangle_{xy}}\right)\delta_{i3} + \tilde{f}_i, \tag{4}$$

$$\partial_t \tilde{\theta}_i + \tilde{u}_j \partial_j \tilde{\theta} = \partial_j \pi_j^{\Delta} \tag{5}$$

where $\tilde{u}_i$ $(i = 1, 2, 3)$ refer to the filtered velocity components in the three Cartesian directions (horizontal: x, y, and vertical: z), $\tilde{\theta}$ represents the filtered potential temperature, and $\tilde{p}^*$ denotes the dynamic modified pressure field. This is defined as $\tilde{p}^* = \tilde{p} + \frac{1}{3}\tau_{kk}^{\Delta} + \frac{1}{2}\tilde{u}_j\tilde{u}_j$, where the first term is the kinematic pressure, the second term is the trace of the subgrid scale (SGS) momentum flux and the last term derives from the rotational form of the convective term. In Eq. 4, the coupling term $g\left(\frac{\tilde{\theta}-\langle\tilde{\theta}\rangle_{xy}}{\langle\tilde{\theta}\rangle_{xy}}\right)\delta_{i3}$ results from the Boussinesq approximation where $\langle\,\rangle_{xy}$ represents a horizontal average, and δ_{ij} is the Kronecker-delta operator. The flow is driven by a geostrophic forcing, imposed using the body force term $\tilde{f}_i = (\tilde{u}_2 - V_G)\nu_G\delta_{i1} - (\tilde{u}_1 - U_G)\nu_G\delta_{i2}$, where (U_G, V_G) are the horizontal geostrophic velocity components, and $\nu_G = 10^{-4}$ Hz is the geostrophic frequency at a latitude of 43.3° N.

The deviatoric part of the SGS momentum flux is written using the eddy-viscosity approach and may be written as $\tau_{ij}^{\Delta,d} = \tau_{ij}^{\Delta} - \frac{1}{3}\tau_{kk}^{\Delta}\delta_{ij} = -2\nu_T\tilde{S}_{ij}$, where $\nu_T = (C_S\Delta)^2|\tilde{S}|$ is the turbulent eddy viscosity, $\tilde{S}_{ij} = \frac{1}{2}\left(\partial_j\tilde{u}_i + \partial_i\tilde{u}_j\right)$ is the resolved strain rate tensor, and C_S is the Smagorinsky coefficient (Smagorinsky 1963; Lilly 1967). This coefficient is computed dynamically using the Lagrangian scale-dependent dynamic model of Bou-Zeid et al. (2005). Similarly for temperature, the SGS temperature diffusion is given by $\pi_j^{\Delta} = \nu_T/Pr_{sgs}\partial_j\tilde{\theta} = (D_S\Delta)^2|\tilde{S}|\partial_j\tilde{\theta}$, where the coefficient D_S is computed dynamically using a Lagrangian scale-dependent dynamic model for scalars (Calaf et al. 2011).

The numerical implementation is based on Albertson and Parlange (1999), later modified by Bou-Zeid et al. (2005), Calaf et al. (2011), and Margairaz et al. (2018). This pseudo-spectral code treats the horizontal derivatives in Fourier space, the vertical derivatives are computed using second-order finite differences on the vertically staggered grid, and the second-order Adam–Bashforth scheme is used for time integration. The lateral boundary conditions are, as a result, periodic. The top boundary conditions are prescribed using a stress-free-lid condition for the horizontal velocity ($\partial_z \tilde{u}_i = 0, i = 1, 2$) and a constant temperature gradient corresponding to the initial strength of the capping inversion ($\partial_z \widetilde{\theta} = cst$). The non-penetration condition ($\tilde{w} = 0$) is imposed on the vertical velocity at the top and bottom of the domain. Monin–Obukhov similarity theory (MOST) (Monin and Obukhov 1954) is used for the bottom boundary condition for the horizontal velocity and temperature. The latter gives a formulation for the surface shear stress and vertical heat flux. The drag from the underlying surface is entirely modelled through the logarithmic wind profile for rough surfaces (von Kármán 1931; Prandtl 1932) corrected for atmospheric stability through MOST. The surface friction velocity u_*, related to the shear stress, is given by

$$u_*^2 = \left[\frac{\kappa}{\ln\left(\frac{\Delta z/2}{z_0}\right) + \psi_m\left(\frac{\Delta z/2}{L}\right)} \right]^2 \left(\hat{\tilde{u}}_1^2(x, y, \Delta z/2) + \hat{\tilde{u}}_2^2(x, y, \Delta z/2) \right), \quad (6)$$

where $\hat{\tilde{u}}_i$ is the velocity field filtered a second time at $2\Delta_{LES}$ and sampled at $\Delta z/2$ where $\Delta_{LES} = \sqrt{\Delta x \Delta y}$ is the horizontal grid size and Δz is the vertical grid size. The aerodynamic roughness length is denoted by z_0 and $\kappa = 0.4$ is the von Kármán constant. The stability correction function of momentum ψ_m is based on Brutsaert (2005) and depends on atmospheric stability assessed by the local Obukhov length $L = -\dfrac{u_*^3 \theta_S}{\kappa g q_s}$. Here, θ_S is the surface temperature, g is the acceleration due to gravity, and q_s denotes the kinematic surface heat flux (Brutsaert 1982). The wall shear stress is then dynamically projected over the horizontal directions using the unit direction vector of the horizontal velocity sampled at $z = \Delta z/2$ and filtered at $2\Delta_{LES}$ (Bou-Zeid et al. 2004; Hultmark et al. 2013).

Similarly, the vertical kinematic sensible heat flux is computed as

$$q_s = \frac{\left[\theta_s(x, y) - \tilde{\theta}(x, y, \Delta z/2)\right]}{\left[\ln\left(\frac{\Delta z/2}{z_{0s}}\right) + \psi_s\left(\frac{\Delta z/2}{L}\right)\right]} \kappa u_*, \quad (7)$$

where ψ_s is the stability correction function for the temperature and z_{0s} is the thermal roughness length, which is specified as $z_{0s} = 0.1 z_0$. The corresponding vertical derivatives of the horizontal velocities and temperature are imposed at the first grid point of the vertically staggered grid following Albertson and

Parlange (1999). This framework was developed for idealized homogeneous surfaces. We are aware of the limitations of the surface parametrization (Basu and Lacser 2017), however, it is also known that this approach provides acceptable results in the case of non-homogeneous conditions (Bou-Zeid et al. 2004; Stoll and Porté-Agel 2006).

3.2 Study Cases

The unstable nature of the boundary layer is established by initially setting the air temperature 5 K lower than the mean surface temperature. The simulations are separated into two sets to study the differences between heterogeneous and homogeneous surfaces. In the first set, a total of seven configurations are considered, all with a homogeneous surface temperature fixed at a value of $\theta_S = 290$ K, and for which the geostrophic wind speed has been increased from 1 to 15 m s^{-1} (i.e., $U_g = 1, 2, 3, 4, 6, 9, 15$ m s^{-1}). Hereafter, these homogeneous cases are referred to as HM-X, where X indicates the geostrophic wind speed corresponding case (see Table 1). In the second set, the surface temperature is distributed amongst square patches, where the temperature of each patch is determined by sampling a Gaussian distribution with a mean temperature of 290 K and a standard deviation of 5 K. In this case, three different patch sizes were considered (i.e., $l_h = 800$, 400, and 200 m). The sizes of the heterogeneities were chosen to be of similar size ($l_h/l_d \approx 1$), half the size ($l_h/l_d \approx 1/2$), and about a quarter of the size ($l_h/l_d \approx 1/4$) of the largest flow motions within the represented thermal boundary layer, assuming that this is of the order of the boundary-layer height ($l_d \sim z_i$). Further, these heterogeneities are typically not resolved in NWP models. These cases have also been studied for the different geostrophic wind speeds indicated above, and hereafter are referred to as HT-X-sYYY, where X indicates the corresponding geostrophic wind speed, and sYYY refers to the size of the patches (e.g., HT-1-s800 would be the heterogeneous case with patches of 800 m, and forced with $U_g = 1$ m s^{-1}). Additionally, for the case with larger patches, three different random distributions of the patches have been considered to evaluate the potential effect of a given surface distribution for all geostrophic wind speeds. This is further indicated with the indicator v_i with $i = 1, 2, 3$. Therefore, in this second set of study cases a total of 35 different configurations have been considered (see Table 1). Figure 2 shows the surface temperature distributions used for the different heterogeneous surface conditions. These temperature distributions emulate the surface thermal conditions observed in Morrison et al. (2017), where measurements of the surface temperature were taken with a thermal camera at the SLTEST site of the US Army Dugway Proving Ground in Utah, USA. This is an ideal site with uniform roughness and a large unperturbed fetch, where surface thermal heterogeneities are naturally created by differences in surface salinity.

In all studied cases, the surface roughness is assumed homogeneous, with $z_0 = 0.1$ m, and representative of a surface with sparse forest or farmland

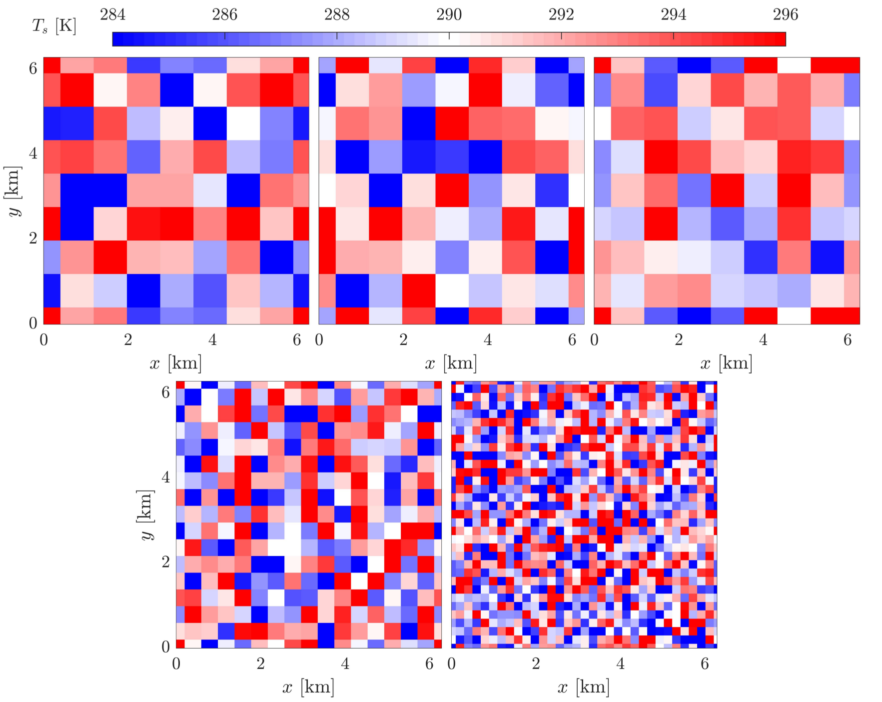

Fig. 2 Surface temperature distributions for the different patches cases. On top: the three 800 m patches (HT-X-s800.v_i). On bottom, left to right: 400 m patches (HT-X-s400), and 200 m patches (HT-X-s200)

with many hedges (Brutsaert 1982; Stull 1988). The initial boundary-layer height is set to z_i = 1000 m. The temperature profile is initialized with a mean air temperature of 285 K. At the top of the initial boundary layer, a capping inversion of 1000 m is used to limit its growth. The strength of this inversion is fixed at $\Gamma = 0.012$ K m^{-1}. The atmospheric boundary layer (ABL) is considered dry and the latent heat flux is neglected in all cases. Further, in all simulations, the surface heat flux is computed using MOST, as explained in Sect. 3.1, where the surface temperature is kept constant in time throughout the simulations. Thus, there is no feedback from the atmosphere to the surface as the surface temperature does not cool down or warm up with local changes in velocities. As a consequence, the ABL gradually warms up as the simulations progress, and hence becomes less convective over time. However, the runs are not long enough for this to be significant. In addition, to ensure a degree of homogeneity within each patch and a certain degree of validity of MOST, note that even for the heterogeneous cases with the fewest amount of grid points per patch, a minimum of eight grid points is granted in each horizontal direction. The domain size is set to $(L_x, L_y, L_z) = (2\pi, 2\pi, 2)$ km at a grid size of $(N_x, N_y, N_z) = (256, 256, 256)$ resulting in a horizontal resolution of $\Delta x = \Delta y = 24.5$ m and a vertical grid spacing of $\Delta z = 7.8$ m. A

Table 1 Summary of the study cases and the corresponding most relevant simulation statistics for 30-min averages. The homogeneous cases are referenced as HM, and cases with heterogeneous surfaces are referred to as HT. In the case of the 800 m patches, the statistics for all three cases are very similar. Thus, HT-X-s800.v_i is presented as representative of all three cases. The proprieties presented in the table are the geostrophic forcing velocity (U_g), the boundary-layer height (z_i), the Obukhov length (L), the stability factor ($-z_i/L$), the friction velocity (u_*), the temperature scale (θ_*), the planar-averaged surface heat flux $\langle\overline{(w'\theta')_S}\rangle$), and the convective velocity scale (w_*). The boundary-layer height and the Obukhov length have been rounded up to the nearest m. The stability factor has been rounded up to the nearest integer

Name	U_g	z_i	L	$-z_i/L$	u_*	θ_*	$\langle\overline{(w'\theta')_S}\rangle$	w_*	w_*/u_*
	m s^{-1}	m	m	-	m s^{-1}	K	m K s^{-1}	m s^{-1}	-
HM-1	1	1313	−4	332	0.17	0.52	0.09	1.44	8.58
HM-2	2	1305	−6	223	0.19	0.45	0.09	1.43	7.54
HM-3	3	1289	−11	114	0.23	0.36	0.08	1.42	6.05
HM-4	4	1281	−20	65	0.28	0.29	0.08	1.41	5.02
HM-6	6	1273	−44	27	0.37	0.23	0.08	1.42	3.83
HM-9	9	1297	−97	13	0.49	0.18	0.09	1.44	2.96
HM-15	15	1328	−266	5	0.71	0.14	0.10	1.49	2.11
HT-1-s800.v_i	1	1422	−2	715	0.16	0.97	0.16	1.75	10.80
HT-2-s800.v_i	2	1383	−3	431	0.19	0.81	0.15	1.73	9.20
HT-3-s800.v_i	3	1359	−6	232	0.23	0.64	0.14	1.70	7.53
HT-4-s800.v_i	4	1344	−10	133	0.27	0.51	0.14	1.67	6.28
HT-6-s800.v_i	6	1336	−24	56	0.35	0.37	0.13	1.63	4.72
HT-9-s800.v_i	9	1344	−67	20	0.49	0.26	0.13	1.62	3.34
HT-15-s800.v_i	15	1359	−196	7	0.69	0.18	0.13	1.62	2.34
HT-1-s400	1	1487	−1	3433	0.10	1.57	0.15	1.01	10.52
HT-2-s400	2	1463	−2	897	0.15	1.06	0.16	0.99	6.47
HT-3-s400	3	1452	−4	397	0.20	0.79	0.16	0.94	4.76
HT-4-s400	4	1434	−8	170	0.26	0.58	0.15	0.90	3.50
HT-6-s400	6	1406	−22	63	0.35	0.40	0.14	0.88	2.51
HT-9-s400	9	1390	−62	22	0.48	0.27	0.13	0.83	1.73
HT-15-s400	15	1404	−197	7	0.70	0.18	0.13	0.76	1.08
HT-1-s200	1	1439	−1	1741	0.12	1.28	0.15	0.93	7.74
HT-2-s200	2	1434	−2	933	0.15	1.04	0.15	0.89	6.02
HT-3-s200	3	1430	−4	377	0.20	0.77	0.15	0.83	4.17
HT-4-s200	4	1434	−8	180	0.25	0.59	0.15	0.79	3.12
HT-6-s200	6	1402	−23	61	0.35	0.40	0.14	0.75	2.13
HT-9-s200	9	1374	−65	21	0.48	0.26	0.13	0.70	1.45
HT-15-s200	15	1383	−207	7	0.70	0.18	0.12	0.63	0.89

timestep of $\Delta t = 0.1$ s is used to ensure the stability of the time integration. This set-up is very similar to that used by Salesky et al. (2017).

The two sets of simulations span a large range of geostrophic forcing conditions, allowing the study of the effect on the structure of the convective boundary layer (CBL) above a patchy surface compared to a homogeneous surface. The range of U_g covers values between 1 m s^{-1} and 15 m s^{-1}. The procedure used to spin up the simulations is the following: a spin-up phase of four hours of real time is used to achieve converged turbulent statistics, which is then followed by an evaluation phase. During the latter, running averages are computed for the next hour of real time. Statistics have been computed for averaging times of 5 min to 1 h, showing statistical convergence at 30-min averages with negligible changes between the 30-min and the 60-min averages.

Table 1 presents a summary of the simulation statistics for the homogeneous and heterogeneous surface cases. The values of the Obukhov length $L = -\dfrac{u_*^3\theta_S}{\kappa g \overline{(w'\theta')_S}}$, the stability parameter $-z_i/L$, the convective velocity $w_* = \left[\dfrac{g}{\bar{\theta}_S} z_i \overline{(w'\theta')_S}\right]^{\frac{1}{3}}$, and the temperature scale $\theta_* = \left[\dfrac{g}{\bar{\theta}_S} z_i\right]^{-\frac{1}{3}} \left[\overline{(w'\theta')_S}\right]^{\frac{2}{3}}$ have been obtained using the planar averages of the 30-min averages of the friction velocity u_* (from Eq. 6), the sensible heat flux $\overline{(w'\theta')_S}$ (from Eq. 7) and the height of the boundary layer z_i. The simulations cover a wide range of atmospheric stability regimes ranging from $-z_i/L < 5$ to $-z_i/L > 700$, and hence spanning from near neutral to highly convective scenarios.

4 Quantification of Surface Thermal Heterogeneity Effects on the Atmospheric Boundary Layer

As a first step of this investigation, Sect. 4.1 presents a quantitative analysis of the effect of the surface thermal heterogeneities on the ABL flow field, considering the impact of increasing geostrophic forcing. Section 4.2 quantifies the contribution of the dispersive flux over the entire ABL and evaluates the dependence with the corresponding averaging time used to compute the dispersive fluxes. Sect. 4.3 examines the contribution of dispersive fluxes in the surface layer, and evaluates its dependence on the size of the averaging area at a specific height.

4.1 Impact of Surface Thermal Heterogeneities on the Flow Field

As a first step of this analysis, Fig. 3 presents instantaneous spatial fluctuations of the vertical velocity and temperature at a height of 100 m ($\approx 1/10\, z_i$). The instantaneous snapshots for the homogeneous cases (Figs. 3a, b) are useful to understand the effect of increasing geostrophic forcing. In the case corresponding to a low wind speed ($U_g = 1$ m s^{-1}, Fig. 3a), the expected convective cells can be observed, both in the velocity and temperature fields. These convective open cells have a diameter of 2–4 km, corresponding to observations made in the CBL (Konrad 1970; Weckwerth et al. 1999; Bennett et al. 2010). As the geostrophic wind speed is increased ($U_g = 15$ m s^{-1}, Fig. 3b), the structure of the flow is transformed from a convective-cell geometry into a roll structure. The transition from cell to roll structure is related to the increase in shear stress, which destroys the original convective-cell structure. To quantify this transition, Salesky et al. (2017) developed a metric based on the two-point correlation function of the vertical velocity in cylindrical coordinates $R_{ww}(r_\eta, r_\phi, z)$, where r_η is the radial lag, r_ϕ is the angular lag, and z is the height above the ground. This method detects the angular dependencies present in the roll-type convection using the statistical range of the two-point correlation function. The statistical range, defined as

$$R(r_\eta) = \max_{r_\phi} \big[R_{ww}(r_\eta, r_\phi, z)\big] - \min_{r_\phi} \big[R_{ww}(r_\eta, r_\phi, z)\big], \tag{8}$$

will be large for the roll-type convection and small for the cell-type convection. Following this observation, the roll factor can be defined as

$$\mathcal{R} = \max_{r_\eta} \big[R(r_\eta) | r_\eta / z_i \leq 0.5\big], \tag{9}$$

where the radial lag is cut at $z/z_i = 0.5$ because only large, convective structures are of interest. Using this metric, the cases presented in Fig. 3 have a roll factor of $\mathcal{R} \approx 0.1$ for $U_g = 1$ m s^{-1} and $\mathcal{R} \approx 0.3$ for $U_g = 15$ m s^{-1}, matching the conceptual structure defined in Salesky et al. (2017).

Interestingly, the original convective-cell structure is also modified when the flow is overlaid on a thermally-heterogeneous surface. In this case (Fig. 3c), the convective-cell structure adjusts to the thermal patches at the surface. The instantaneous snapshot of the flow field illustrates how cells merge into larger cells, or break into much smaller cells or updrafts that concentrate forming boarders that surround the larger cells. In this case, the characteristic length scale of the larger fluid motions (l_d) is related to the length scale of the surface thermal heterogeneities (l_h) or larger, if there are nearby patches with similar surface temperature. For smaller updrafts, the characteristic length scale is of the order of 200 m to 400 m, compatible with the observations made by Bennett et al. (2010) over Oklahoma. This length scale is smaller than the individual surface temperature patch sizes (l_h). Subsequently, when the geostrophic wind speed increases ($U_g = 9$ m s^{-1}), the convective-cell structure is destroyed, similar to the homogeneous case. Furthermore, the footprint of the surface temperature patches is no longer evident in the temperature and velocity fields (Fig. 3d). In this case, the roll factor is larger than 0.25, very similar to what was obtained in the case of a homogeneous surface temperature. It is therefore clear that under conditions of moderate geostrophic forcing the impact of the surface thermal heterogeneities is blended, and its corresponding impact on the flow structure is reduced.

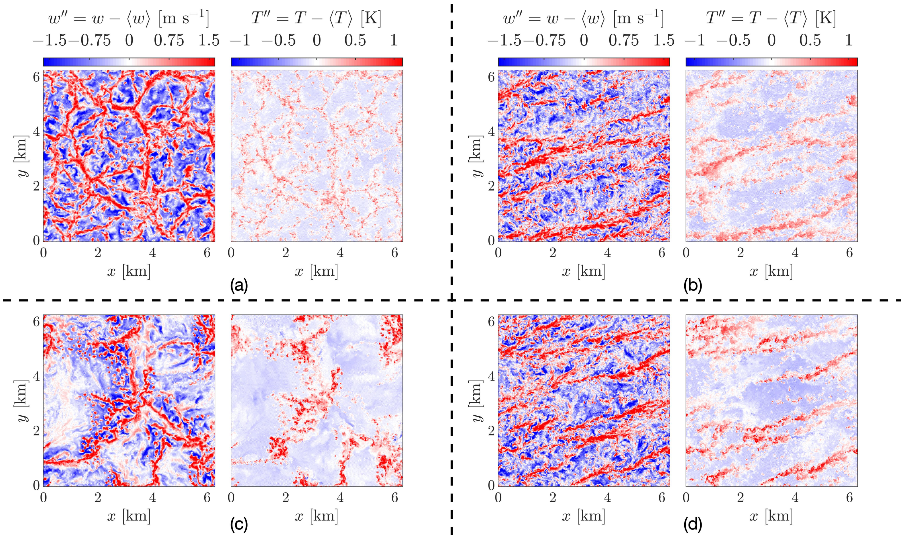

Fig. 3 Instantaneous spatial fluctuations of the two-dimensional-horizontal $(x - y)$ fields at $z = 100$ m and $t = 4$ h of the vertical velocity $w'' = w(x, y, z, t) - \langle w \rangle_{x,y}(z, t)$ and temperature $T'' = T(x, y, z, t) - \langle T \rangle_{x,y}(z, t)$. The top subfigures (a, b) correspond to cases over a homogeneous surface with a geostrophic wind speed of (a) $U_g = 1$ m s^{-1} (HM-1) and (b) $U_g = 15$ m s^{-1} (HM-15). The bottom subfigures (c, d) correspond to the corresponding heterogeneous cases for the 800-m patches with a geostrophic wind speed of (c) $U_g = 1$ m s^{-1} (HT-1-s800.v_1) and (d) $U_g = 15$ m s^{-1} (HT-15-s800.v_1)

4.2 Dispersive Fluxes in the Atmospheric Boundary Layer

The progressive blending of thermal heterogeneities with increasing geostrophic wind speed can be better observed through the magnitude of the dispersive fluxes computed for the study cases introduced in Sect. 3.2. To quantify the relative importance of the dispersive flux with respect to the total sensible heat flux, the following metric is introduced:

$$\frac{\int_0^{z_i} Q_{disp}(\xi)\,\mathrm{d}\xi}{\int_0^{z_i} \Big[Q_{Reynolds}(\xi) + Q_{SGS}(\xi) + Q_{disp}(\xi)\Big]\,\mathrm{d}\xi} = \frac{\int_0^{z_i} Q_{disp}(\xi)\,\mathrm{d}\xi}{\int_0^{z_i} Q_{tot}(\xi)\,\mathrm{d}\xi}, \tag{10}$$

where Q_{disp} represents the dispersive flux, $Q_{Reynolds}$ is the planar-averaged resolved turbulent sensible heat flux, and Q_{SGS} is the planar-averaged SGS contribution of the sensible heat flux. Because the fluxes are integrated over the full ABL column, this metric represents the integral fraction of the total sensible heat flux that arises from the dispersive fluxes. Note that the boundary-layer height is taken as the height where the total sensible heat flux crosses the zero value before the capping inversion. Figure 4 illustrates these results for values of fluxes computed for a 30-min time period. In this figure, the contribution of the dispersive fluxes for the heterogeneous surface cases progressively decreases as the geostrophic wind speed increases (which is a result of the increased blending as illustrated above) until the effect of

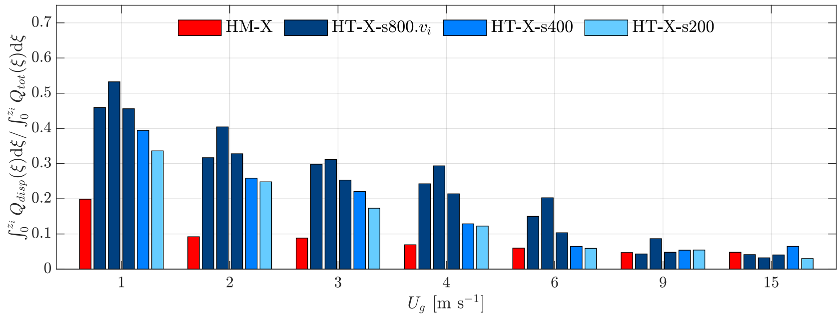

Fig. 4 Integral fraction of sensible heat flux accounted for by the dispersive fluxes as a function of geostrophic wind speed when averaged over a 30-min time period. (red) indicates the homogeneous cases; (dark-blue) heterogeneous cases with 800-m patches; (blue) heterogeneous cases with 400-m patches; (light-blue) heterogeneous cases with 200-m patches

the surface thermal heterogeneities does not have an impact on the dispersive fluxes. These results seem to indicate the existence of two differentiated regimes. In the first regime, the contribution of the dispersive fluxes is intrinsic to the surface thermal heterogeneities, and hence represent a measure of the impact of the surface on the flow. In the second regime, the dispersive fluxes are fully due to the turbulent coherent structure, or consistency in time related to the surface induced shear. For the homogeneous cases, the dispersive fluxes arise from the coherent structures that remain in similar locations for the averaging period and their contributions decrease with increasing geostrophic wind speed. At low wind speeds, the dispersive fluxes arise from the persistent Rayleigh–Bénard convective cells. In the second regime, the dispersive fluxes are the result of coherent, turbulent structures induced by the shear. In both cases, in the limit of very long time averages, these would become zero for the homogeneous surface conditions. It is also interesting to see that the transition between the convective regime and the second regime occurs faster for the homogeneous cases.

In situations where the dispersive fluxes are related to the surface thermal heterogeneities, the dispersive fluxes can account for more than 40% of the total sensible heat flux for the HT-1-s800.v_i cases, about 40% for HT-1-s400, and about 33% for the HT-1-s200 case when integrated over the full ABL depth. Also, from the results presented in Fig. 4, it can be observed that different surface spatial arrangements of patches with the same size (l_h) and standard deviation (cases HT-1-s800.v_i) lead to very similar dispersive flux contributions. This is an important result because it indicates that the dispersive flux fraction is independent of any specific spatial distribution of thermal heterogeneities.

Because the definition of the dispersive fluxes is dependent on its time-averaging operation (as explained in Sect. 2), it is important to evaluate the dependence of the dispersive flux fraction on the time-averaging operation. Hence, Fig. 5 illustrates the integral fraction of sensible heat flux accounted for by the dispersive fluxes as a function of time-averaging period, and geostrophic wind speed. In Figs. 5a and b, the geostrophic forcing is weak and hence the contribution of the dispersive fluxes is related to the surface thermal heterogeneities. There is a maximum decrease in dispersive flux contribution with increasing time-averaging period from 5–30 min ranging between 30% and 50%. Note that this decrease is much smaller ($< 15\%$) for averaging periods greater than 20 min. Furthermore, the contribution of the dispersive fluxes remains relevant even at 60-min averages, ranging between 30% and 45% for the weakest geostrophic wind speed ($U_g = 1$ m s^{-1}) and between 10% and 30% for a moderate geostrophic wind speed ($U_g = 3$ m s^{-1}). Energy balance closure studies have demonstrated similar dependence on the averaging time (Foken 2006; Charuchittipan et al. 2014).

Further analysis of the contributions of the dispersive fluxes in the homogeneous cases indicate that the dispersive fluxes are appreciable at all geostrophic wind speeds for short averaging times. In this case, the dispersive fluxes are interpreted as being generated by coherent spatial distribution of turbulent flow that are persistent over the short averaging times. When the geostrophic forcing is strong and blends the surface heterogeneity, the dispersive fluxes account for the structure of the time-resilient and shear-dominated turbulent flow. This is illustrated well in Fig. 5c, cases where $U_g = 9$ m s^{-1} and the effect of the surface heterogeneities is mostly blended. In these cases, the corresponding values of the dispersive fluxes found for large averaging times are small, but not negligible.

To further explore this direct relationship between the dispersive fluxes and the surface imposed thermal heterogeneities, Fig. 6 is a scatter plot comparing the contribution of the dispersive flux for the homogeneous case with the heterogeneous cases (Fig. 6a), as well as the corresponding correlation between the surface-temperature distribution and the air temperature at $z/z_i = 0.05$ (Fig. 6b). It can be observed that the correlation is maximum for lowest geostrophic wind speed and decreases with increasing wind speed. In particular, the cases with the largest correlations between the surface and air temperature correspond well with the cases in which the integral contribution of the dispersive fluxes is much larger than those found over the homogeneous surfaces. This is illustrated in Fig. 6b. This important relationship between the surface and air temperature at $z/z_i = 0.05$ is interpreted as being responsible for the relevant contribution of the dispersive flux to the overall heat flux (see Fig. 6a). Further, we believe that this result could be exploited to develop simplified parametrizations of the dispersive fluxes based on remotely sensed surface temperature measurements. In the case of the largest geostrophic wind speed, this correlation is reduced to a minimum ($< 50\%$), and the dispersive fluxes match well with those measured over homogeneous surfaces indicating that they are unrelated to the surface thermal patchiness.

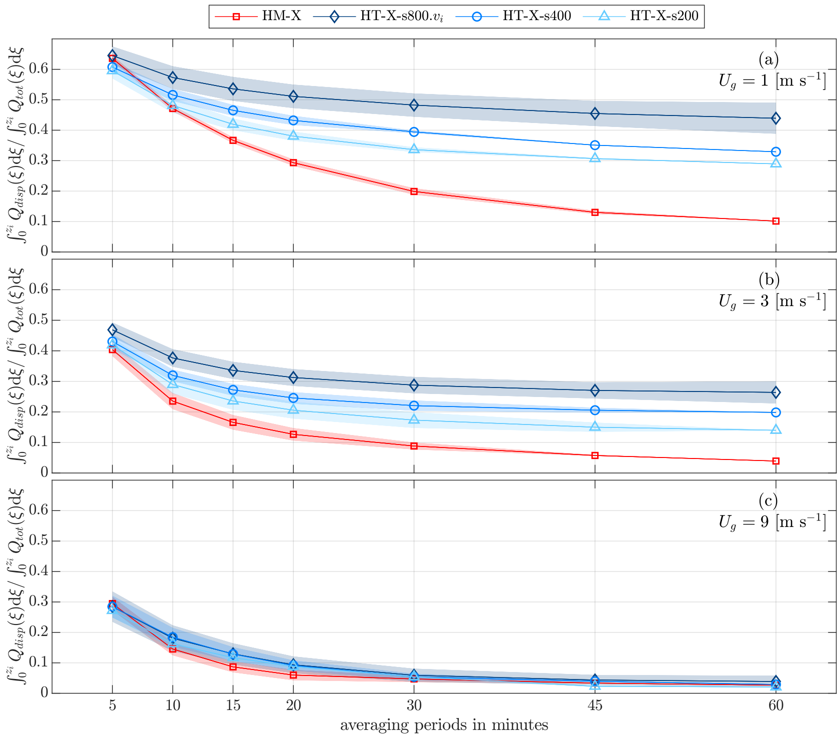

Fig. 5 Integral fraction of sensible heat flux accounted by the dispersive fluxes as a function of averaging time, and geostrophic wind intensity (top $U_g = 1$ m s^{-1}, middle $U_g = 3$ m s^{-1}, and bottom $U_g = 9$ m s^{-1}). (red) indicates the homogeneous cases; (dark-blue) heterogeneous cases with 800-m patches; (blue) heterogeneous cases with 400-m patches; (light-blue) heterogeneous cases with 200-m patches

4.3 Dispersive Fluxes in the Surface Layer

Figure 7 provides additional information on the vertical distribution of the dispersive fluxes throughout the boundary layer. Specifically, Fig. 7 shows vertical profiles of the integral fraction of the dispersive flux with respect to the total sensible heat flux for 30-min time averages as a function of height,

$$\frac{\int_0^z Q_{disp}(\xi)\,\mathrm{d}\xi}{\int_0^z \Big[Q_{Reynolds}(\xi) + Q_{SGS}(\xi) + Q_{disp}(\xi)\Big]\,\mathrm{d}\xi} = \frac{\int_0^z Q_{disp}(\xi)\,\mathrm{d}\xi}{\int_0^z Q_{tot}(\xi)\,\mathrm{d}\xi}. \tag{11}$$

Note that in this case, both the numerator and the denominator represent the integral up to a given height z. The ratio of the dispersive flux over the total sensible turbulent heat flux represents the averaged cumulative contribution of the dispersive flux up to a given height. Hence, based on this definition, the dispersive flux contribution is zero at the surface and increases quickly with height until reaching saturation at around $z/z_i \approx 0.3$–0.5, depending on the

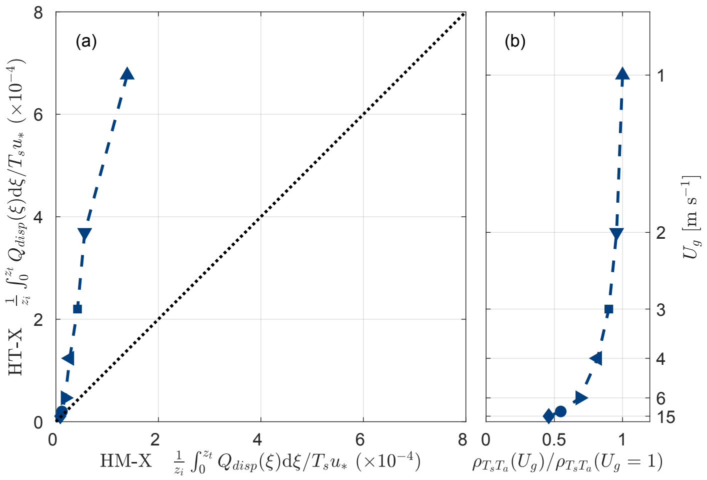

Fig. 6 (a) Comparison between the contribution of the dispersive fluxes over the full ABL for the cases with a heterogeneous thermal surface (averaged over the different patch sizes) and the case with a homogeneous thermal surface. (b) Correlation between the surface temperature and air temperature at $z/z_i = 0.05$ as a function of the geostrophic wind speed. Each point corresponds to the geostrophic forcing reported on the right vertical axis as represented by the different style of markers

geostrophic wind speed. In this figure, the horizontal black line illustrates the height above which the contribution of the dispersive fluxes does not change by more than 10%. From the profiles, it can be observed that close to the surface ($z/z_i \approx 0.02$) the contribution of the dispersive fluxes can be as much as 5–10% for a spatial average spanning the full domain. Similar to what had been observed in Fig. 4, the net contribution to the total sensible heat flux by the dispersive fluxes for the different surface conditions diminishes with increasing geostrophic forcing until there is no difference between the homogeneous and heterogeneous cases (i.e. all vertical profiles overlap). This result is also in line with the two regimes discussed above, one in which the dispersive fluxes are directly correlated with the surface thermal heterogeneities, and another one in which they are related to the surface shear-induced turbulent structure. These two regimes can be related to the LES study of Inagaki et al. (2006), which showed fluxes originating from two different processes: thermally-induced circulations and turbulent organized structures. Additionally, Fig. 7 shows the ratio of the contribution of the dispersive fluxes to that of the turbulent contribution (dotted lines). This complementary illustration of the results further illustrates that dispersive fluxes are most important for low geostrophic wind speed cases, potentially being of equal or larger value than the turbulent fluxes. In fact, for weak geostrophic forcing, the ratio of the dispersive flux to the turbulent flux can be up to three times bigger for heterogeneous cases than the homogeneous case. In contrast, under strong geostrophic forcing, this difference between homogeneous and heterogeneous

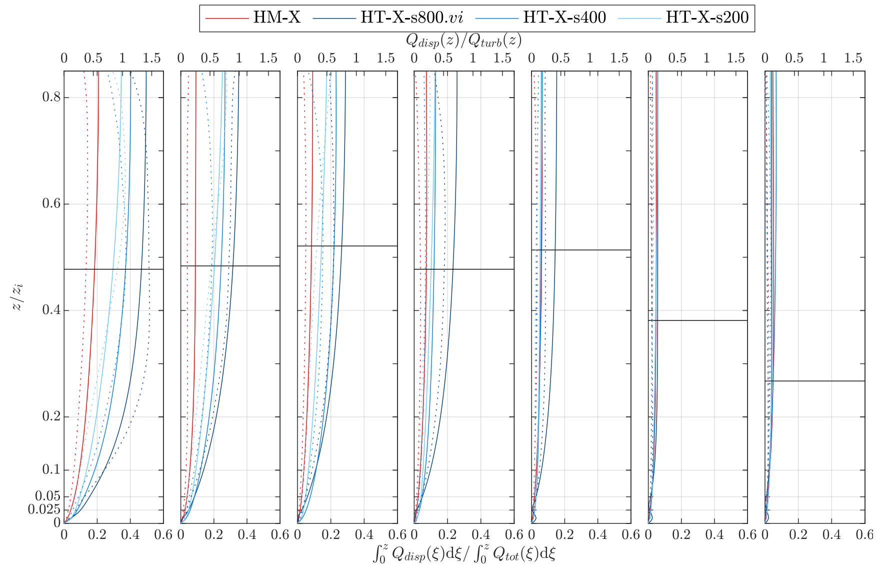

Fig. 7 Continuous lines represent the vertical profiles of the integral fraction of sensible heat flux accounted for by the dispersive fluxes for 30-min averages as a function of geostrophic wind speed (from left to right: U_g = 1, 2, 3, 4, 6, 9, 15 m s^{-1}). The horizontal black line illustrates the height above which the contribution of the dispersive fluxes does not change by more than 10%. The dotted lines illustrate the local ratio of the dispersive flux to the total sensible heat flux at a given height z (with respect to the top axes)

cases falls below 15% compared to weaker forcing. In addition, even close to the surface ($z/z_i \approx 0.02$) the dispersive-flux contribution is non-negligible. The existence of large-scale structures close to the surface has been demonstrated though field measurements by Eder et al. (2015). These structures might be responsible for the behaviour of the fluxes observed here.

The results presented to this point have been horizontally averaged over the full domain. Therefore, while providing a measure of the overall contribution of the dispersive fluxes in the bulk ABL transport processes as a function of differential geostrophic and surface forcings, this approach does not provide an answer to the a priori opening hypotheses of this work, namely: 1. Can dispersive fluxes provide a means of capturing the effect induced by the unresolved surface heterogeneities in near-future NWP resolutions ($\sim$ 100 m)? 2. Can dispersive fluxes explain the non-closure of the surface energy budget?

To address these questions, a wide range of different horizontal-averaging length scales (Δ_{CS}) are used in the averaging operator $\langle\cdot\rangle$ that defines the dispersive fluxes. Figure 8 provides a measure of the contribution of the dispersive fluxes versus the turbulent fluxes as a function of the horizontal-averaging length scale. In this figure, the horizontal-averaging length scale is normalized by a ‘dispersive’ integral length scale. Results are shown at the study height of 32 m. This height corresponds to the fourth grid point in the LES domain in the vertical direction, in which the potential numerical artifacts introduced by

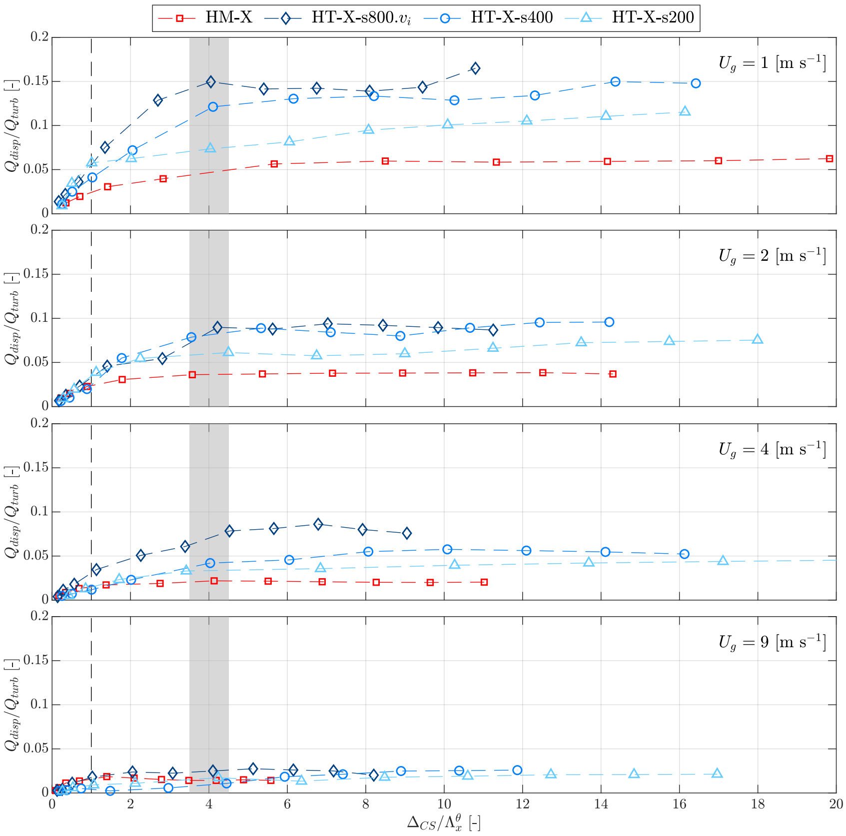

Fig. 8 Ratio of the dispersive fluxes versus the turbulent fluxes as a function of averaging surface defined by the Control Surface area Δ_{CS} and the dispersive integral length scale for temperature Λ_x^θ at $z = 32$ m. From top to bottom, the geostrophic forcing increases. The dashed line illustrates where $\Delta_{CS}/\Lambda_x^\theta = 1$, and the grey-shaded bar indicates the averaging area wherein the contribution from the dispersive fluxes and the turbulent fluxes reach equilibrium

the LES wall-boundary conditions have been diffused, and also approximately corresponds to the height of the first grid point in NWP models. Therefore, this is where surface parametrizations would be applied in NWP models.

The dispersive integral length scale (Λ_x^θ, dispersive integral length scale for temperature in the x-direction) characterizes the footprint of the surface heterogeneities on the time-averaged flow. This length scale is computed through the correlation of the spatial fluctuations of the time-averaged temperature field ($\bar{\theta}''$) in the x-direction, similar to what traditionally is done to compute the turbulent integral length scale (Pope 2000). This dispersive length scale (Λ_x^θ) is assumed to have a magnitude similar to the surface-heterogeneity length scale l_h shown in Fig. 1. Results indicate that when the ratio of the averaging control surface characteristic length scale Δ_{CS} to Λ_x^θ is approximately

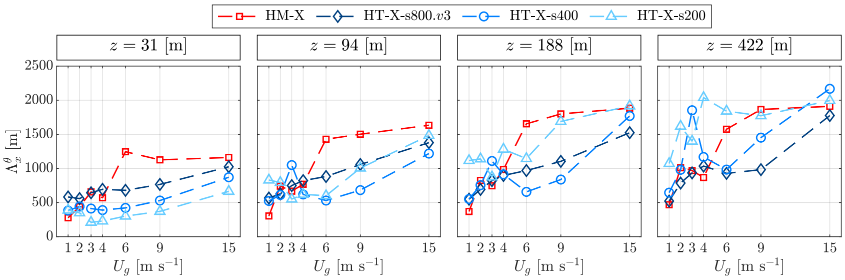

Fig. 9 Values of the dispersive integral length scale for temperature in the streamwise direction Λ_x^θ as a function of increasing height (left to right) and increasing geostrophic wind speed

4, one obtains the full contribution of the dispersive fluxes, with only minor changes to the fluxes as Δ_{CS} is increased.

The dispersive integral length scale is of similar magnitude to the size of the surface thermal patches when the geostrophic forcing is weak, as indicated in Fig. 9. This measure remains smaller than the physical size of the numerical domain ($2\pi\, z_i$) even for the largest patches. Therefore, an immediate consequence of these results is that the findings presented in Sect. 4 remain valid, despite having been averaged over the full LES domain, since the asymptotic behaviour is reached before needing to average over the whole domain. Also, from Fig. 8, it is worth noting that the dispersive-flux contribution to tends to zero when the averaging control surface is small in comparison to the size of the thermal heterogeneity length scale, which is equivalent to the hypothesis illustrated in Fig. 1 and described in Sect. 1 when $l_d >> l_h$ (i.e.the flow field feels the surface as homogeneous). Alternatively, when averaging over the correct length scales, the dispersive fluxes can contribute between 3 and 15% of the turbulent fluxes at moderate to low wind speeds. This result, although from a highly idealized scenario, already provides an initial preliminary response to the earlier hypothesis of whether dispersive fluxes could account for the 5–10% of energy that is traditionally missing when computing surface energy budgets (Foken 2008; Stoy et al. 2013). This result requires further confirmation either using experimental data or more realistic numerical simulations.

5 Spectral Structure of the Turbulent Flow

We further investigate the relationship between the flow structure (modulated by the surface heterogeneities and the mean flow) and the dispersive fluxes with the goal of aiding the future development of ASL parametrizations. First, we interrogate the turbulent fluctuations of vertical velocity and temperature, as well as their covariance for weak and strong geostrophic forcing, respectively. To describe the dominant structure in the flow, spectrograms are used, following Jacob and Anderson (2017) and Salesky and Anderson (2018). This representation of turbulent pre-multiplied two-dimensional spectra provides a good description of the structure of the flow. This method allows us to analyze the interaction between the different scales of motion and the resolved turbulent heat flux, noting that it is agnostic to the subgrid component of the heat flux.

The fluctuations used to compute the spectra are based on 30 instantaneous snapshots taken every 2 min with the 30-min averages subtracted. The two-dimensional spectra are computed by binning over shells of constant wavenumber $k_h = \sqrt{k_x^2 + k_y^2}$ and smoothed by averaging over the 30 snapshots (Wyngaard 2010).

Figure 10 presents spectrograms of turbulent fluctuations for the heterogeneous cases under weak and strong geostrophic forcing. Under weak forcing, the main peak of the vertical velocity fluctuations is located in the upper part of the ABL at scales between $\lambda_h = 1000$ m and $\lambda_h = 4000$ m. In addition, the small eddies ($\lambda_h < 1000$ m) close to the surface ($z < 100$ m) are less energetic than under stronger forcing. Similar spectrograms were reported by Salesky and Anderson (2018) and correspond to cell-type convection. The different surface conditions are modulating the small eddies in the first 100 m of the ABL. It can be observed that the smaller patches tend to generate smaller and more energetic eddies closer to the surface. The increasing geostrophic forcing stretches these coherent structures and redistributes the energy between different scales. Although the height of the main peak remains approximately the same, its location shifts towards larger scales. At the same time, the small eddies close to the surface are more energetic than for the weaker geostrophic wind speed. Also, no modulation from the surface heterogeneities is observed. A similar behaviour was also observed for the homogeneous surface cases although it is not represented here in Fig. 10 for the sake of clarity.

In contrast, the temperature fluctuations show the presence of a double hump in the lower 100 m of the ABL for all the heterogeneous surface cases. This feature is particularly evident under strong geostrophic forcing. It is worth noting that the valley in between has a similar scale as the size of the patches. This characteristic feature is not present in the homogeneous cases (not shown). Instead, these cases only have a small hump for short wavelengths. This observation seems to indicate that the double hump observed can be explained by a combination of surface fluctuations induced by the flow ($\lambda_h \lesssim \Delta$) and fluctuations produced by the surface patchiness ($\lambda_h \gtrsim \Delta$). In addition, the lower hump shifts towards smaller scales under strong forcing, increasing the valley between the two humps.

In comparison, the structure of the covariance does not seem to be significantly affected by the surface thermal heterogeneity. The weak geostrophic forcing cases exhibit very similar structures among the different surface conditions, where the dominant peak can be found between $z = 100$ m and $z = 1000$ m. As with the vertical velocity fluctuations, increasing geostrophic forcing seems to shift the dominant structure towards larger scales that are higher in the ABL. In this case, the peak is found around $z = 500$ m and at a wavelength of $\lambda_h > 4$ km. A similar observation can also be made on the homogeneous

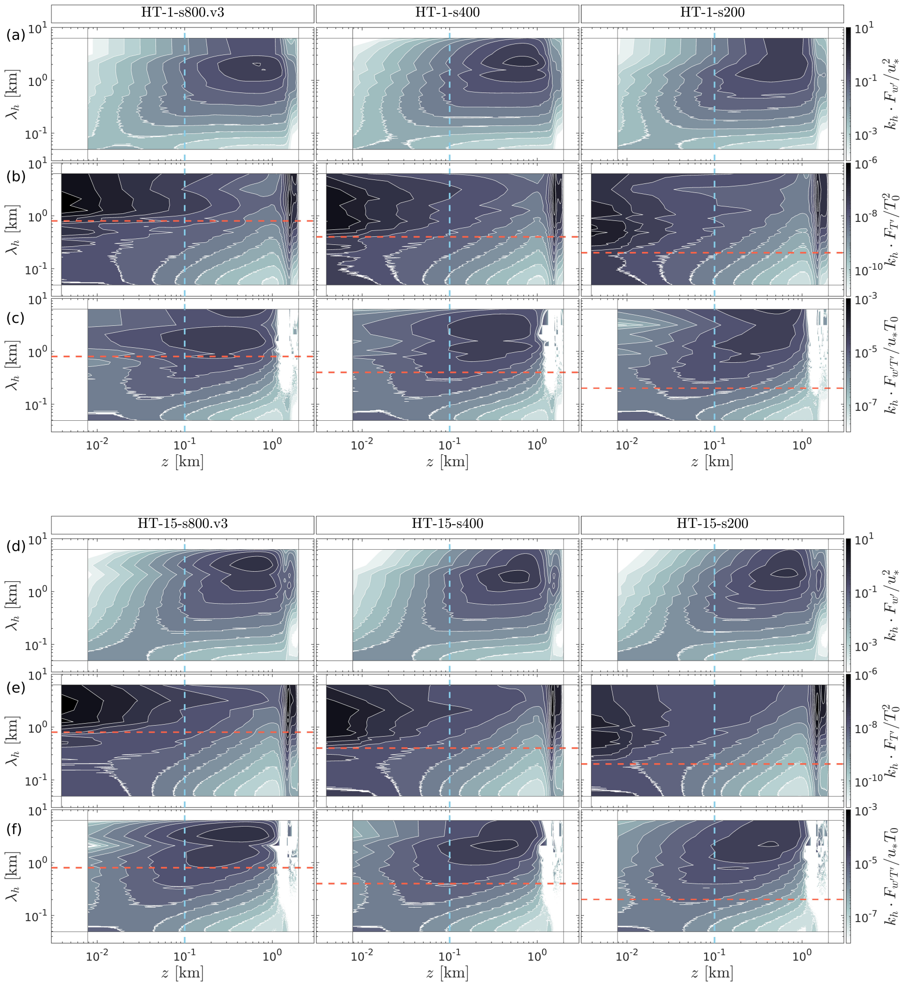

Fig. 10 Spectrograms of turbulent fluctuations for different patch sizes at $U_g = 1$ m s^{-1} (a, b, c) and $U_g = 15$ m s^{-1} (d, e, f). The x-axis represents the height z in km; the y-axis represents the streamwise wavelength $\lambda_h = 2\pi/k_h$ in km. The lines show the limits of the domain in the vertical and horizontal directions. The verical dashed line (blue) shows the 100 m height corresponding to the top of the ASL. The horizontal dashed line (red) corresponds to the patch size $\lambda_h = \Delta$. For each geostrophic forcing, the panels are: (a, d) vertical velocity $F_{w'}$, (b, e) potential temperature $F_{T'}$, (c, f) cospectra of the vertical velocity and potential temperature $F_{w'T'}$. The spectra are averaged over 30 instantaneous snapshots

case (not shown). Hence, the spectral representation of the turbulent heat flux does not appear t be significantly modulated by the surface patchiness. Although some of the subgrid contributions might be missing in these figures, the imprint of the thermal surface heterogeneity is imposed on the flow and the heat exchanges mechanisms are clearly observed.

Overall, the turbulent spectrograms reveal that similar features are present in both the resolved flow field (w') and the resolved turbulent heat flux ($w'T'$) with minor modulations due to the surface conditions. However, the temperature spectrograms show the footprint of surface heterogeneities on the turbulent fluctuations with a second structure in the large scales. It is worth noting that the turbulent fluctuations of temperature do not appear in the turbulence kinetic energy equation but only appear in the heat flux budget equation in the buoyancy term (Stull 1988). Hence, the surface heterogeneities have a limited impact on the production of turbulence kinetic energy and the balance between shear and buoyant production.

Next, we investigate the structure of dispersive fluctuations. Following Raupach and Shaw (1982), the dispersive fluctuations are defined as $\bar{w}'' = \bar{w} - \langle \bar{w} \rangle$ with $\bar{w}$ representing time averaging and $\langle \bar{w} \rangle$ representing horizontal spatial averaging. Figure 11 illustrates the spectrograms of vertical velocity dispersive fluctuations ($\bar{w}'' = \bar{w} - \langle \bar{w} \rangle$), temperature dispersive fluctuations ($\bar{T}'' = \bar{T} - \langle \bar{T} \rangle$), and their corresponding covariance ($\bar{w}''\bar{T}''$).

The spectrograms of the vertical velocity dispersive fluctuations show that the flow is significantly influenced by the geostrophic forcing. Under weak forcing, the dominant structures of the vertical velocity lie between $z = 300$ m and $z = 1000$ m, and span between $\lambda_x = 1$ km and $\lambda_x = 6$ km, independent of the surface thermal patch sizes. In contrast, under strong geostrophic wind speeds, the spatial fluctuations of the time-averaged velocity are small, as traditionally expected. The dominant structures are located between $\lambda_h = 1$ km and $\lambda_h = 2$ km, and are mostly observed in the upper region of the ABL.

In contrast, the spectrograms of the dispersive temperature fluctuations are affected both by the size of the patches and by the geostrophic forcing. First, the size of the underlying patches correlates well with the dominant spectral length scales. Although these structures seem to be mainly concentrated in the ASL, they can reach up to $z = 600$ m in height, spanning most of the CBL. As the geostrophic wind speed increases, strong mixing significantly reduces the span in height of the dominant structures. As expected, the corresponding dispersive cospectra exhibit a behaviour resulting from the combined responses observed in the vertical velocity and temperature dispersive fluctuations. Therefore, the overlapping in wavelength of the structures present at weak geostrophic forcing leads to considerable dispersive fluxes. On the contrary, for high geostrophic wind speeds, the is no region of overlap between the characteristic wavelengths of vertical velocity and temperature dispersive fluctuations. Hence, the cospectra have small values under high wind speed conditions. These observations explain the contribution of the dispersive fluxes reported in Fig. 4, because the integration of the cospectra over the wavelengths at a given height yields the dispersive contribution at that height. A similar integration can be made for the resolved turbulent flux.

To further understand how the cospectra of the turbulent heat flux and the dispersive flux are modified by the different surface thermal conditions and mean wind speeds, the scaling of the corresponding turbulent and dispersive cospectra is analyzed next. As expected from turbulence theory (Kaimal and

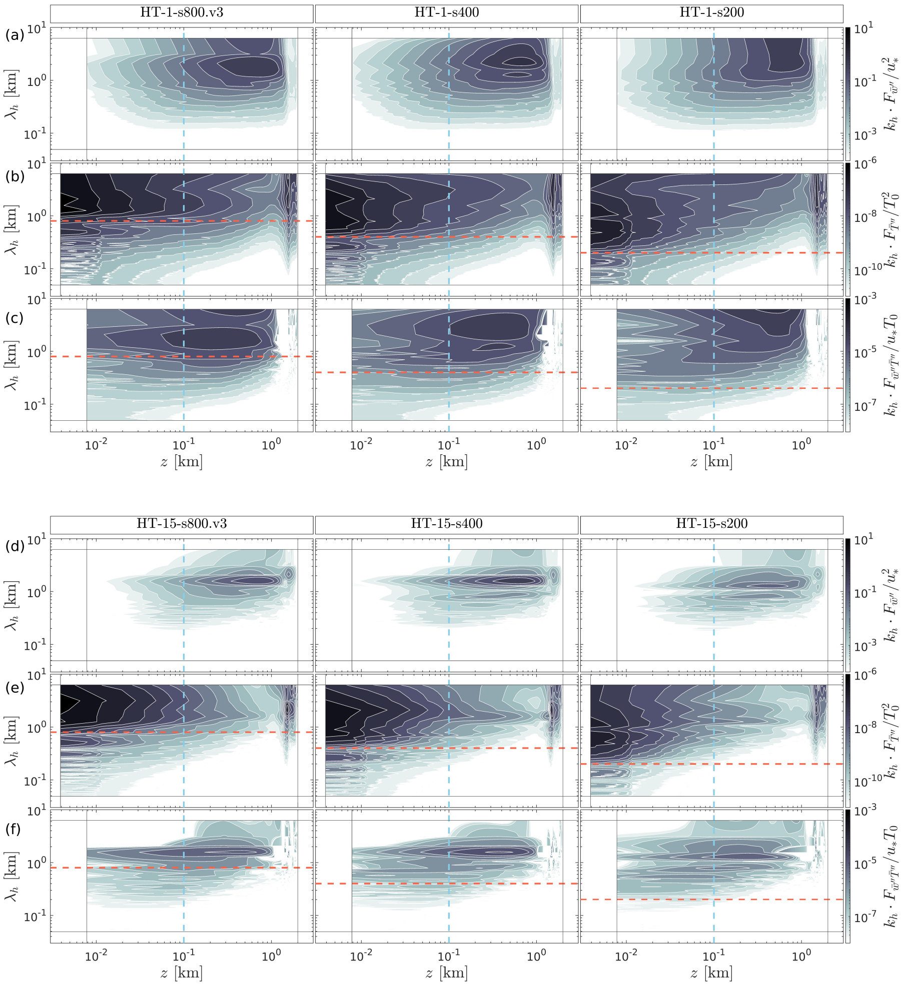

Fig. 11 Spectrograms of the time-averaged spatial fluctuations for the different patch sizes at $U_g = 1$ m s^{-1} (a, b, c) and $U_g = 15$ m s^{-1} (d, e, f). The x-axis represents the height z in km; the y-axis represents the streamwise wavelength $\lambda_h = 2\pi/k_h$ in km. The lines show the limits of the domain in the vertical and horizontal and directions. The vertical dashed line (blue) shows the 100 m height corresponding to the top of the ASL. The horizontal dashed line (red) corresponds to the patch size $\lambda_h = \Delta$. For each geostrophic forcing, the panels are: (a, d) vertical velocity $F_{\bar{w}''}$, (b, e) potential temperature $F_{\bar{T}''}$, (c, f) cospectra of the vertical velocity and potential temperature $F_{\bar{w}''\bar{T}''}$. The spectra are averaged over 7 30-min periods

Finnigan 1994; Pope 2000; Li et al. 2015) the cospectra of the turbulent fluctuations scale with $k^{-7/3}$. This can be observed in Fig. 12a where the cospectrum corresponding to the homogeneous configuration is presented.

The cospectra of the heterogeneous cases also scale with $k^{-7/3}$ through the high wavenumber region of the spectra ($k_h z_i > 10$). In this region, both the homogeneous and the heterogeneous cases are very similar. Hence, within the

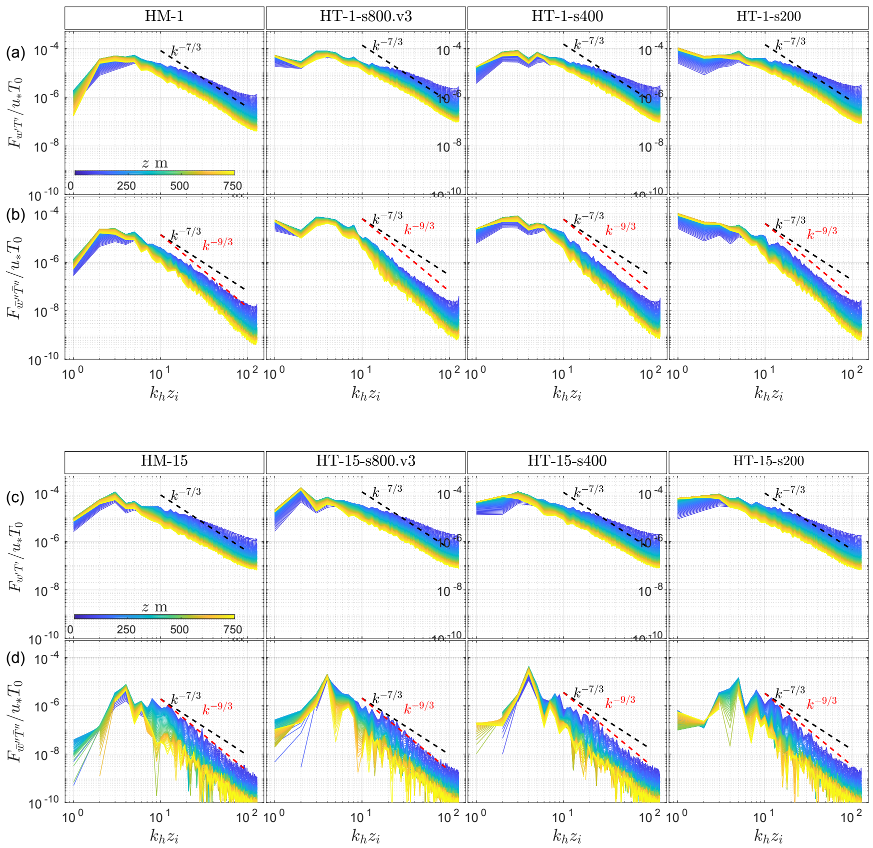

Fig. 12 Cospectra of the vertical velocity and potential temperature for the different patch sizes at $U_g = 1$ m s^{-1} (a, b) and $U_g = 15$ m s^{-1} (c, d). Black-dashed line represent the traditional $k^{-7/3}$ scaling of the turbulent flux cospectre, red-dashed line shows the $k^{-9/3}$ scaling observed in the dispersive flux cospectra. The colours represent the height above the ground where blue is the lowest level (50 m) and yellow correspond to a level around 750 m. For each geostrophic forcing, the panels are: (a, c) turbulent fluctuations, (b, d) time-averaged spatial fluctuation

mixed layer, the small-scale turbulent fluctuations follow the same dynamics. However, the low wavenumber part of the cospectra ($k_h z_i < 10$) seems to be affected by the surface patchiness with the heterogeneous cases having more energy at these scales.

In contrast, the dispersive flux cospectra exhibit notable differences between the weak and strong forcing. The weak forcing cases show a $k^{-7/3}$ scaling to the surface similar to the resolved turbulent heat flux where the lower boundary condition dictates the dynamics of the flow. However, the scaling shifts progressively towards a $k^{-9/3}$ scaling higher up in the ABL. In the case of $U_g = 1$ m s^{-1}, this $k^{-9/3}$ scaling can be observed for $z > 200$ m. Also, the way in which this shift occurs seems to be independent of surface patch size.

In comparison, the change between the two different scalings does not seem to occur in the cospectra of the dispersive flux at strong geostrophic forcing where a $k^{-9/3}$ scaling dominates through the whole ABL. Figure 12d shows that the cospectra are similar for all the surface conditions. Also, the smaller amplitudes of the cospectra confirm that the dispersive flux is less significant in the strong geostrophic forcing cases, which agrees well with the results presented earlier in the analysis developed based on flow statistics.

6 Discussion

In the early 1980s, the concept of dispersive fluxes was introduced to account for momentum fluxes arising in vegetated canopies as a result of first time averaging and then spatial averaging the flow field (Raupach and Shaw 1982; Finnigan 1985; Raupach et al. 1986). This process can lead to persistent flow heterogeneities in time. In the present study, dispersive fluxes are reinterpreted as arising from the spatial-averaging operation that explicitly represents critical processes dependent on heterogeneity induced in the flow by surface thermal patchiness. This can be easily generalized to any process inducing persistent flow heterogeneities. From the analysis presented, two main results are extracted: the dispersive-flux contribution to the total energy exchange in the ABL can be important, and dispersive fluxes are associated with the topology of the underlying surface heterogeneity, or with the persistent turbulent structure of the ABL flow (depending on the geostrophic forcing and the time-averaging operation).

Further, results seem to indicate the existence of two regimes where the role of the dispersive fluxes is modulated by different effects. The first effect is one in which dispersive fluxes are driven by surface heterogeneities. The other is a regime where dispersive fluxes are driven by long-lived coherent structures of atmospheric turbulence in high-shear conditions. Therefore, differentiation based on these two regimes could facilitate developing new parametrizations. This is a topic of ongoing research.

In addition, spectral analysis revealed that the footprint of surface patchiness can be clearly found in the time-averaged quantities, especially the air temperature. The presence of this footprint shows the interaction between the ABL flow and the surface patchiness. This is especially relevant under weak geostrophic forcing, where shear does not dominate over buoyancy. Furthermore, large dispersive fluxes result from the combination of reduced blending of the mean temperature spatial fluctuations and increased mean vertical velocity spatial fluctuations. Regarding the $k^{-9/3}$ scaling slope observed in the cospectra of the dispersive fluctuations, further investigations are underway. These first results indicate that substantial dispersive-flux contributions are observed when the cospectra follow a $k^{-9/3}$ scaling and that the new scaling presented in this paper is not linked to turbulence, as it is different than $k^{-7/3}$. However, at this stage it is unclear how the different scaling is linked to the dispersive flux and what mechanism leads to the new power-law exponent. However, we believe that this newly apparent scaling represents an opportunity to model the dispersive fluxes over heterogeneous land surfaces.

While the results illustrate new physical interpretation of the interaction between surface thermal heterogeneities and the atmospheric flow, it is also important to realize that the simulations used remain quite canonical, and hence present certain limitations. For example, the simulations are forced through an imposed surface temperature, which eventually leads to different atmospheric stability values for the different study cases. While this could be an important limitation in a study that focused on a one-to-one intercomparison of cases, it does not affect the interpretation of the results. This is because the aim has focused on illustrating that dispersive fluxes can be relevant in realistic ABL conditions, and that these are dependent on geostrophic forcing, heterogeneity length scale, and time averaging. The reason for forcing the flow with an imposed surface temperature, instead of an imposed surface flux, as done in Salesky et al. (2017), is because the design of the simulations was inspired from recent experimental measurements using a thermal camera over an alkaline palya in Utah's West Desert at the U.S. Army Dugway Proving Ground (Morrison et al. 2017). Further, coupling of the surface with the atmosphere through a strong one-way coupling limits the potential feedback that the land surface might have on the atmospheric flow. Further, while some previous LES studies have demonstrated that scalar transport due to turbulent organized structures can be measure by the dispersive fluxes even over homogeneous surfaces (Kanda et al. 2004), other studies have also shown that the residual value measured by the dispersive fluxes can be the result of locking large coherent structures induced by the limited size of the LES domain and the periodicity of the numerical algorithm as indicated in Munters et al. (2016). To check on this potential pitfall, a test simulation with a four times larger domain was also run for the HT-1-s800 study case. In this case, results corresponded well with those obtained with the smaller domain, indicating that in the heterogeneous cases the LES domain size did not affect the results. It is also important to realize that the numerical cost associated with such large LES configurations makes the analysis presented here unfeasible given the large number of required study cases.

7 Conclusions

We presented an LES study of the influence of surface thermal heterogeneities on the atmospheric boundary-layer flow as a function of geostrophic forcing, and as a function of thermal patch size. For the first time, we propose the use of dispersive fluxes as a measure of the footprint that these surface thermal heterogeneities have on the flow. Results illustrate that under weak geostrophic forcing, dispersive fluxes can account for up to 40% of the total sensible heat flux at about $0.1z_i$, with a value of 5 to 10% near the surface. These dispersive fluxes provide an indirect measure of the footprint that thermal heterogeneities have on the flow. Under stronger geostrophic forcing, heterogeneities are blended, changing the structure of the flow, and reducing the dispersive fluxes to approximately 5%. In this latter case, dispersive fluxes provide a measure of the coherent structure of the mean flow induced by the ground surface shear stress.

Finally, an innovative spectral analysis of the dispersive contributions has shed light on the influence of both the geostrophic forcing and the different surface conditions on the spatial fluctuations of the vertical velocity and temperature. These observations indicate that large dispersive fluxes arise from the combined effect of the limited blending of surface temperatures and large vertical velocity structures created by the buoyancy forces. Finally, the cospectral analysis also revealed the existence of a new power-law scaling for the dispersive fluxes under weak shear forcing.

Acknowledgements The authors would like to thank Prof. Katul (Duke University) for fruitful discussions and Prof. Anderson (UT Dallas) for the suggestion to consider using the spectrogram representation. This project has been developed with the support of the U.S. National Science Foundation grant number PDM-1649067. Marc Calaf also acknowledges the Mechanical Engineering Department at the University of Utah for start-up funds, and the Center for High Computing Performance (CHPC) at the University of Utah for computing hours. This work used the Extreme Science and Engineering Discovery Environment (XSEDE), which is supported by National Science Foundation grant number ACI-1548562. The authors declare no conflict of interest.

References

Albertson JD, Parlange MB (1999) Natural integration of scalar fluxes from complex terrain. Adv Water Resour 23:239–252

Ament F, Simmer C (2006) Improved representation of land-surface heterogeneity in a non-hydrostatic numerical weather prediction model. Boundary-Layer Meteorol 121(1):153–174

Arola A (1999) Parameterization of turbulent and mesoscale fluxes for heterogeneous surfaces. J Atmos Sci 56(4):584–598

Avissar R (1991) A statistical-dynamical approach to parameterize subgrid-scale land-surface heterogeneity in climate models. Surveys in Geophysics 12(1-3):155–178

Avissar R (1992) Conceptual aspects of a statistical-dynamical approach to represent landscape subgrid-scale heterogeneities in atmospheric models. J Geophys Res 97(D3):2729–2742

Avissar R, Pielke RA (1989) A parameterization of heterogeneous land surfaces for atmospheric numerical models and its impact on regional meteorology. Mon Weather Rev 117(10):2113–2136

Bailey BN, Stoll R (2013) Turbulence in sparse, organized vegetative canopies: A large-eddy simulation study. Boundary-Layer Meteorol 147(3):369–400

Basu S, Lacser A (2017) A cautionary note on the use of MoninObukhov similarity theory in very high-resolution large-eddy simulations. Boundary-Layer Meteorol 163(2):351–355

Beare RJ (2014) A length scale defining partially-resolved boundary-layer turbulence simulations. Boundary-Layer Meteorol 151(1):39–55
Beljaars ACM, Holtslag AAM (1991) Flux parameterization over land surfaces for atmospheric models. J Appl Meteorol 30(3):327–341
Bennett LJ, Weckwerth TM, Blyth AM, Geerts B, Miao Q, Richardson YP (2010) Observations of the evolution of the nocturnal and convective boundary layers and the structure of open-celled convection on 14 June 2002. Mon Weather Rev 138(7):2589–2607
Blyth EM (1995) Using a simple SVAT scheme to describe the effect of scale on aggregation. Boundary-Layer Meteorol 72(3):267–285
Blyth EM, Dolman AJ, Wood N (1993) Effective resistance to sensible and latentheat flux in heterogeneous terrain. Q J R Meteorol Soc 119(511):423–442
Bou-Zeid E, Meneveau C, Parlange MB (2004) Large-eddy simulation of neutral atmospheric boundary layer flow over heterogeneous surfaces: Blending height and effective surface roughness. Water Resour Res 40(2):1–18
Bou-Zeid E, Meneveau C, Parlange MB (2005) A scale-dependent Lagrangian dynamic model for large eddy simulation of complex turbulent flows. Phys Fluids 17(2):025,105
Brutsaert W (1982) Evaporation into the atmosphere. Springer Netherlands, Dordrecht
Brutsaert W (2005) Hydrology. Cambridge University Press, Cambridge
Calaf M, Meneveau C, Meyers J (2010) Large eddy simulation study of fully developed wind-turbine array boundary layers. Phys Fluids (1994-present) 22(1):015,110
Calaf M, Meneveau C, Parlange MB (2011) Large Eddy Simulation study of a fully developed thermal wind-turbine array boundary layer. in: Kuerten H., Geurts B., Armenio V., Frhlich J. (eds) Direct and large-eddy simulation VIII, ERCOFTAC Series, vol 15. Springer Netherlands, Dordrecht
Charuchittipan D, Babel W, Mauder M, Leps JP, Foken T (2014) Extension of the averaging time in eddy-covariance measurements and its effect on the energy balance closure. Boundary-Layer Meteorol 152(3):303–327
Cheng H, Castro IP (2002) Near wall flow over urban-like roughness. Boundary-Layer Meteorol 104(2):229–259
Claussen M (1990) Area-averaging of surface fluxes in a neutrally stratified, horizontally inhomogeneous atmospheric boundary layer. Atmospheric Environment Part A General Topics 24(6):1349–1360
Claussen M (1991) Estimation of areally-averaged surface fluxes. Boundary-Layer Meteorol 54(4):387–410
De Roo F, Mauder M (2018) The influence of idealized surface heterogeneity on virtual turbulent flux measurements. Atmospheric Chemistry and Physics 18(7):5059–5074
Eder F, Schmidt M, Damian T, Träumner K, Mauder M (2015) Mesoscale eddies affect near-surface turbulent exchange: Evidence from lidar and tower measurements. J Appl Meteorol Clim 54(1):189–206

Finnigan JJ (1985) Turbulent transport in flexible plant canopies. In: The Forest-Atmosphere Interaction, Springer Netherlands, Dordrecht, pp 443–480

Finnigan JJ (2000) Turbulence in plant canopies. Ann Rev Fluid Mech 32(1):519–571

Foken T (2006) 50 years of the Monin-Obukhov similarity theory. Boundary-Layer Meteorol 119(3):431–447

Foken T (2008) The energy balance closure problem: An overview. Ecol Appl 18(6):1351–1367

Giometto MG, Christen A, Meneveau C, Fang J, Krafczyk M, Parlange MB (2016) Spatial characteristics of roughness sublayer mean flow and turbulence over a realistic urban surface. Boundary-Layer Meteorol 160(3):425–452

Hultmark M, Calaf M, Parlange MB (2013) A new wall shear stress model for atmospheric boundary layer simulations. J Atmos Sci 70(11):3460–3470

Inagaki A, Letzel MO, Raasch S, Kanda M (2006) Impact of surface heterogeneity on energy imbalance: A study using LES. J Meteorol Soc Jpn 84(1):187–198

Jacob C, Anderson W (2017) Conditionally averaged large-scale motions in the neutral atmospheric boundary layer: Insights for aeolian processes. Boundary-Layer Meteorol 162(1):21–41

Kaimal JC, Finnigan JJ (1994) Atmospheric boundary layer flows : Their structure and measurement, first edition, Oxford University Press

Kanda M, Inagaki A, Letzel MO, Raasch S, Watanabe T (2004) LES study of the energy imbalance problem with eddy covariance fluxes. Boundary-Layer Meteorol 110(3):381–404

von Kármán T (1931) Mechanical similitude and turbulence. Nachrichten von der Gesellschaft der Wissenschaften zu Gottingen - Fachgruppe I (Mathematik) 5:1–19

Konrad TG (1970) The dynamics of the convective process in clear air as seen by radar. J Atmos Sci 27:1138–1147

Kravchenko A, Moin P (1997) On the effect of numerical errors in large eddy simulations of turbulent flows. J Comput Phys 131(2):310–322

Li D, Bou-Zeid E (2013) Synergistic interactions between urban heat islands and heat waves: The impact in cities is larger than the sum of its parts. J Appl Meteorol Clim 52(9):2051–2064

Li D, Katul GG, Bou-Zeid E (2015) Turbulent energy spectra and cospectra of momentum and heat fluxes in the stable atmospheric surface layer. Boundary-Layer Meteorol 157(1):1–21

Lilly D (1967) Representation of small scale turbulence in numerical simulation experiments. Proceedings of the IBM Scientific Computing Symposium on Environmental Sciences (December):195–210

Margairaz F, Giometto MG, Parlange MB, Calaf M (2018) Comparison of dealiasing schemes in large-eddy simulation of neutrally stratified atmospheric flows. Geosci Model Dev 11(10):4069–4084

Martilli A, Santiago JL (2007) CFD simulation of airflow over a regular array of cubes. Part II: Analysis of spatial average properties. Boundary-Layer Meteorol 122(3):635–654

Mason PJ (1988) The formation of areally-averaged roughness lengths. Q J R Meteorol Soc 114(480):399–420

Mauder M, Desjardins RL, Pattey E, Gao Z, van Haarlem R (2008) Measurement of the sensible eddy heat flux based on spatial averaging of continuous ground-based observations. Boundary-Layer Meteorol 128(1):151–172

Mignot E, Barthelemy E, Hurther D (2009) Double-averaging analysis and local flow characterization of near-bed turbulence in gravel-bed channel flows. J Fluid Mech 618:279–303

Moeng C, Sullivan PP (2015) Large-eddy simulation. In: Encyclopedia of Atmospheric Sciences, Elsevier, pp 232–240

Moltchanov S, Bohbot-Raviv Y, Duman T, Shavit U (2015) Canopy edge flow: A momentum balance analysis. Water Resour Res 51(4):2081–2095

Monin A, Obukhov A (1954) Basic laws of turbulent mixing in the surface layer of the atmosphere. Contrib Geophys Inst Acad Sci USSR 24(151):163–187

Morrison TJ, Calaf M, Fernando HJS, Price TA, Pardyjak ER (2017) A methodology for computing spatially and temporally varying surface sensible heat flux from thermal imagery. Q J R Meteorol Soc 143(707):2616–2624

Munters W, Meneveau C, Meyers J (2016) Shifted periodic boundary conditions for simulations of wall-bounded turbulent flows. Phys Fluids 28(2):025,112

Patton EG, Sullivan PP, Moeng CH (2005) The influence of idealized heterogeneity on wet and dry planetary boundary layers coupled to the land surface. J Atmos Sci 62(7):2078–2097

Poggi D, Katul GG (2008) The effect of canopy roughness density on the constitutive components of the dispersive stresses. Exp Fluids 45(1):111–121

Poggi D, Katul GG, Albertson JD (2004) A note on the contribution of dispersive fluxes to momentum transfer within canopies. Boundary-Layer Meteorol 111(3):615–621

Pope SB (2000) Turbulent flows. Cambridge University Press, Cambridge

Prandtl L (1932) Zur Turbulenten Strömung in Rohren und langs Glätten. Ergebnisse der Aerodynamischen Versuchsanstalt zu Göttingen B. 4:18–29

Raupach MR (1994) Simplified expressions for vegetation roughness length and zero-plane displacement as functions of canopy height and area index. Boundary-Layer Meteorol 71(1-2):211–216

Raupach MR, Shaw RH (1982) Averaging procedures for flow within vegetation canopies. Boundary-Layer Meteorol 22(1):79–90

Raupach MR, Thom AS (1981) Turbulence in and above plant canopies. Annu Rev Fluid Mech 13(1):97–129

Raupach MR, Coppin PA, Legg BJ (1986) Experiments on scalar dispersion within a model plant canopy part I: The turbulence structure. Boundary-Layer Meteorol 35(1-2):21–52

Salesky ST, Anderson W (2018) Buoyancy effects on large-scale motions in convective atmospheric boundary layers: Implications for modulation of near-wall processes. J Fluid Mech 856:135–168

Salesky ST, Chamecki M, Bou-Zeid E (2017) On the nature of the transition between roll and cellular organization in the convective boundary layer. Boundary-Layer Meteorol 163(1):41–68

Smagorinsky J (1963) General circulation experiments with primirive equations. Mon Weather Rev 91(3):99–164

Stoll R, Porté-Agel F (2006) Dynamic subgrid-scale models for momentum and scalar fluxes in large-eddy simulations of neutrally stratified atmospheric boundary layers over heterogeneous terrain. Water Resour Res 42(1):1–18

Stoll R, Porté-Agel F (2009) Surface heterogeneity effects on regional-scale fluxes in stable boundary layers: Surface temperature transitions. J Atmos Sci 66(2):412–431

Stoy PC, Mauder M, Foken T, Marcolla B, Boegh E, Ibrom A, Arain MA, Arneth A, Aurela M, Bernhofer C, Cescatti A, Dellwik E, Duce P, Gianelle D, van Gorsel E, Kiely G, Knohl A, Margolis H, McCaughey H, Merbold L, Montagnani L, Papale D, Reichstein M, Saunders M, Serrano-Ortiz P, Sottocornola M, Spano D, Vaccari F, Varlagin A (2013) A data-driven analysis of energy balance closure across FLUXNET research sites: The role of landscape scale heterogeneity. Agric For Meteorol 171-172:137–152

Stull RB (1988) An Introduction to boundary layer meteorology. Springer Netherlands, Dordrecht

Taylor PA (1987) Comments and further analysis on effective roughness lengths for use in numerical three-dimensional models. Boundary-Layer Meteorol 39(4):403–418

Weckwerth TM, Horst TW, Wilson JW (1999) An observational study of the evolution of horizontal convective rolls. Mon Weather Rev 127(9):2160–2179

Wieringa J (1986) Roughness-dependent geographical interpolation of surface wind speed averages. Q J R Meteorol Soc 112(473):867–889

Wilson NR, Shaw RH (1977) A higher order closure model for canopy flow. J Appl Meteorol 16(11):1197–1205

Wood N, Mason PJ (1991) The influence of static stability on the effective roughness lengths for momentum and heat transfer. Q J R Meteorol Soc 117(501):1025–1056

Wyngaard JC (2004) Toward numerical modeling in the “terra-incognita”. J Atmos Sci 61(14):1816–1826

Wyngaard JC (2010) Turbulence in the atmosphere. Cambridge University Press, Cambridge

Xie ZT, Coceal O, Castro IP (2008) Large-eddy simulation of flows over random urban-like obstacles. Boundary-Layer Meteorol 129(1):1–23

Zhou Y, Li D, Liu H, Li X (2018) Diurnal variations of the flux imbalance over homogeneous and heterogeneous landscapes. Boundary-Layer Meteorol 168(3):417–442